Journal of Computational Physics 396 (2019) 54–71

Contents lists available at ScienceDirect

Journal of Computational Physics

www.elsevier.com/locate/jcp

A high order efficient numerical method for 4-D Wigner equation of quantum double-slit interferences

Zhenzhu Chen [a], Sihong Shao [a,*], Wei Cai [b]

[a] LMAM and School of Mathematical Sciences, Peking University, Beijing 100871, China
[b] Department of Mathematics, Southern Methodist University, Dallas, TX 75275, USA

ARTICLE INFO

Article history:
Received 23 March 2019
Received in revised form 12 June 2019
Accepted 12 June 2019
Available online 21 June 2019

Keywords:
Quantum interference
Wigner equation
Operator splitting
Spectral method
Characteristic method
Double-slit experiment

ABSTRACT

We propose a high order numerical method for computing time dependent 4-D Wigner equation with unbounded potentials and study a canonical quantum double-slit interference problem. To address the difficulties of 4-D phase space computations and higher derivatives from the Moyal expansion of the nonlocal pseudo-differential operator for unbounded potentials, an operator splitting technique is adopted to decompose the 4-D Wigner equation into two sub-equations, which can be computed either analytically or numerically with high efficiency. The first sub-equation contains only a linear convection term in $(\boldsymbol{x}, t)$-space and can be solved with an upwinding characteristic method, while the second involves the pseudo-differential term and can be approximated by a plane wave expansion in $\boldsymbol{k}$-space. By exploiting properties of Fourier transformations, the expansion coefficients for the second sub-equation have explicit forms and the resulting scheme is shown to be unconditionally stable for any high order derivatives in the Moyal expansion, ensuring the feasibility of 4-D Wigner numerical simulations for quantum double-slit interferences. Numerical experiments demonstrate the spectral convergence in $(\boldsymbol{x}, \boldsymbol{k})$-space and provide highly accurate information on the number, position, and intensity of the interference fringes for different types of slits, quantum particle masses, and initial states (pure and mixed).

© 2019 Elsevier Inc. All rights reserved.

1. Introduction

As one of the most important interference experiments in physics, the double-slit experiment has played a key role in optics and quantum mechanics. In his famous Lectures on Physics, Richard Feynman said the quantum double-slit interference is '*impossible, absolutely impossible, to explain in any classical way*', '*has in it the heart of quantum mechanics*', and '*contains the only mystery*' [1]. In classical physics, the first Young's double-slit experiment appeared in 1801 and demonstrated the wave property of light [2]. In modern physics, the double-slit experiment provides evidence for the de Broglie relation of matter. The first quantum interference experiment was performed in 1927 and showed that electrons could display characteristics of both waves and particles [3]. Afterwards, physicists conducted successfully more double-slit interference experiments for large particles, including atoms [4,5], dimers [6], small clusters [7], and even large molecules like C_{60} [8,9]. However, the double-slit interference of larger objects has remained experimentally challenging, despite the development of powerful interferometric techniques for quantum experiments. Fortunately, with the rapid development of computers, there is a

* Corresponding author.
E-mail address: sihong@math.pku.edu.cn (S. Shao).

https://doi.org/10.1016/j.jcp.2019.06.047
0021-9991/© 2019 Elsevier Inc. All rights reserved.

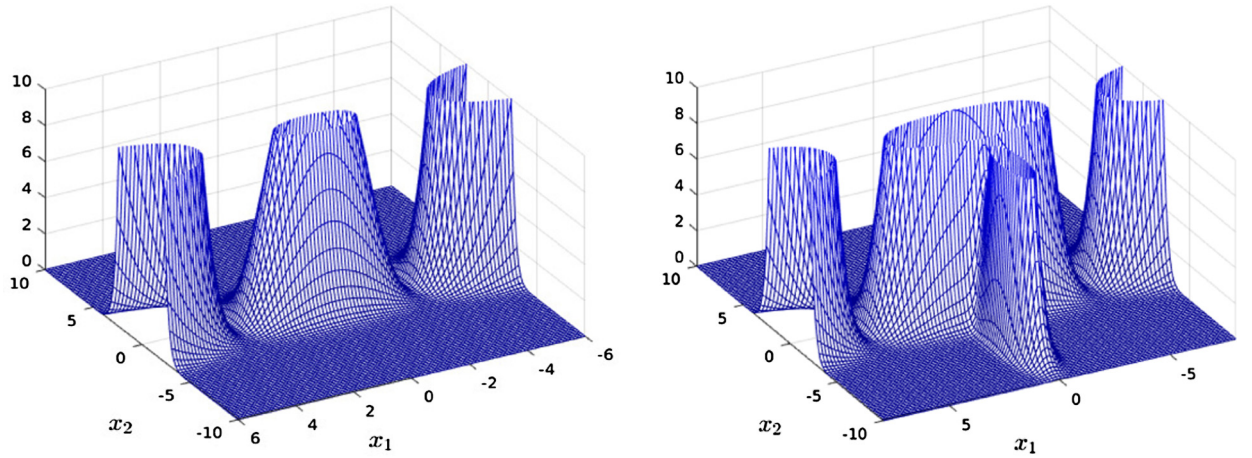

Fig. 1. Two typical double-slit potentials. The left one is described by Eq. (1) with $a = 0.2$, $b = 3$ and $\alpha = \sqrt{2}$. The right one has a central splitter plate in the front and can be modeled by a more general form, see Eq. (6) or (15).

possibility to computationally simulate the quantum interference of larger objects and quantitatively produce meaningful phenomena to help us understand quantum interferences for these objects.

Numerical simulations of quantum double-slit interference have been a long-standing research topic in computational quantum mechanics and may help us living in the classical reality to understand the mysteries of quantum mechanics [10]. In the past decades, several attempts, including the linearized semiclassical initial value representation method [11,12], the Feynman path integral method [13], the Bohmian trajectory method [14,15] and the entangled trajectory method [16,17], have been proposed mainly with two mathematical representations of quantum mechanics. The first three methods mentioned above are based on the Schrödinger wavefunction theory. The linearized semiclassical initial value representation method [11,12] utilizes the semiclassical molecular dynamics to approximate quantum dynamics, therefore cannot fully capture the quantum interference. The Feynman path integral method [13] uses a kernel to approximate the sum of all possible trajectories, while the Bohmian trajectory method [14,15] adopted some kind of approximate trajectories. In contrast, the entangled trajectory method [16,17] is based on the Wigner function in phase space [18] and adopts a representation composed of a finite ensemble of trajectories. Meanwhile, a type of Gaussian approximation is used to deal with the nonlocal pseudo-differential term and, as a result, the negative excursion of the Wigner function, crucial for some quantum behaviors [19,20], is totally neglected there. The present work uses the Wigner function approach to simulate the quantum double-slit interference, and treats both negative and positive excursions on the same footing.

In addition, the Wigner function formalism is chosen out of the following motivations. As a phase space formulation for quantum mechanics, the Wigner function approach bears a close analogy to classical mechanics [21,22] and has been drawing growing attention recently [23,20,24]. As stated in [5], the Wigner function can be viewed in the form of a quasi-probability distribution, thereby yielding a more convenient and direct comparison with physical experiments. And, the Wigner function naturally includes mixed states and provides a unified treatment in dealing with both pure and mixed states [25]. Based on these advantages as well as recent results on highly accurate Wigner simulations, we will develop a high order efficient numerical method for the 4-D Wigner equation for quantum double-slit interferences. To this end, we consider the following double-slit potential (shown in the left plot of Fig. 1)

$$V(x_1, x_2) = a(x_1^2 - b^2)^2 e^{-x_2^2/\alpha^2}, \tag{1}$$

as in [11,12,14,15,17], which consists of a Gaussian barrier along the x_2-direction with a width of α and a double-well in the x_1-direction allowing two open aisles at $x_1 = \pm b$ through the barrier. Here e denotes the base of the natural logarithm.

For realistic simulations, the complexity of the 4-D computation and the higher derivatives in $\boldsymbol{k}$ produced by the Moyal expansion of the unbounded potential bring great challenges. In our previous work [26], an advective-spectral-mixed method for 4-D Wigner equations with localized potential was shown to relax the usual CFL restriction on the time step in $(\boldsymbol{x}, t)$-space and have almost no time step limitation in $(\boldsymbol{k}, t)$-space. Later, a spectral collocation scheme was proposed to deal with the unbounded potential by the Moyal expansion of the pseudo-differential term in 2-D phase space [27]. However, by using the same Moyal expansion to treat the unbounded potential in Fig. 1 for the double-slit interference experiment, the resulting higher derivatives in $\boldsymbol{k}$ create a much stringent time step limitation in $(\boldsymbol{k}, t)$-space such that a long-time 4-D simulation is unaffordable. To resolve this problem, an operator splitting technique will be used to decompose the 4-D Wigner equation into two sub-equations. One is a linear advection equation, which will be solved by a semi-Lagrangian-type characteristic method in $(\boldsymbol{x}, t)$-space, while a Chebyshev expansion in $\boldsymbol{x}$-space is used to handle the inflow boundary condition. The other equation contains the nonlocal pseudo-differential term to be approximated by a plane wave expansion to accurately resolve the oscillations of the Wigner function, and the expansion coefficients can be obtained analytically due to the

nature of Fourier transformation in the pseudo-differential term. The resulting operator splitting scheme will be shown to be spectrally accurate in $(\boldsymbol{x}, \boldsymbol{k})$-space as well as unconditionally stable.

The proposed high order splitting method for the 4-D Wigner equation allows us to simulate the double-slit interference with high accuracy, and obtain detailed information of the interference fringes, such as the number, position, and intensity. The spatial marginal distribution $F(x_1, x_2)$, the angular distribution $P(\theta)$, and the transmission rate $T(t)$ are measured. An investigation on the effect of numerical resolutions on the interference fringes is performed to show the significance of high accuracy. Quantum interference experiments of mixed states and a new double-slit setup (a splitter plate added in front of the double-slit) [28] are also explored numerically in this work.

The rest of this paper is organized as follows. Section 2 gives a brief introduction to the Wigner equation with an emphasis on different forms of the pseudo-differential term. In Section 3, the operator splitting technique is adopted to decompose the 4-D Wigner equation into two sub-equations, both of which can be resolved analytically or efficiently by spectral methods. Section 4 analyzes the conservation property, stability, and convergence of the resulting scheme. Section 5 uses a Gaussian barrier scattering and a harmonic oscillator to benchmark the accuracy, and then simulation of several typical quantum double-slit interference experiments with detailed discussions is given in Section 6. The paper ends in Section 7 with some conclusions and remarks.

2. The 4-D Wigner equation

The Wigner function $f(\boldsymbol{x}, \boldsymbol{k}, t)$ in the $2d$-D phase space $(\boldsymbol{x}, \boldsymbol{k}) \in \mathbb{R}^{2d}$ (d is the dimension of physical space) for the position $\boldsymbol{x}$ and the wavevector $\boldsymbol{k}$, is defined by the Weyl-Wigner transform of the density matrix $\rho(\boldsymbol{x}, \boldsymbol{x}', t) = \sum_i p_i \psi_i(\boldsymbol{x}, t)\psi_i^*(\boldsymbol{x}', t)$ with p_i being the probability of occupying the i-th state as follows

$$f(\boldsymbol{x}, \boldsymbol{k}, t) = \int_{\mathbb{R}^d} \mathrm{d}\boldsymbol{y} \mathrm{e}^{-\mathrm{i}\boldsymbol{k}\boldsymbol{y}} \rho(\boldsymbol{x} + \frac{\boldsymbol{y}}{2}, \boldsymbol{x} - \frac{\boldsymbol{y}}{2}, t), \tag{2}$$

where $\mathrm{i} = \sqrt{-1}$ represents the imaginary unit.

Starting from the quantum Liouville equation, it can be shown that the Wigner function $f(\boldsymbol{x}, \boldsymbol{k}, t)$ satisfies the following time-dependent Wigner equation

$$\frac{\partial}{\partial t} f(\boldsymbol{x}, \boldsymbol{k}, t) + \frac{\hbar \boldsymbol{k}}{m} \cdot \nabla_{\boldsymbol{x}} f(\boldsymbol{x}, \boldsymbol{k}, t) = \Theta_V[f](\boldsymbol{x}, \boldsymbol{k}, t), \tag{3}$$

$$\Theta_V[f](\boldsymbol{x}, \boldsymbol{k}, t) = \frac{1}{\mathrm{i}\hbar} \int \mathrm{d}\boldsymbol{y} \mathrm{e}^{-\mathrm{i}\boldsymbol{k}\boldsymbol{y}} \left[V(\boldsymbol{x} + \frac{\boldsymbol{y}}{2}) - V(\boldsymbol{x} - \frac{\boldsymbol{y}}{2}) \right] \hat{f}(\boldsymbol{x}, \boldsymbol{y}, t), \tag{4}$$

$$\hat{f}(\boldsymbol{x}, \boldsymbol{y}, t) = \frac{1}{(2\pi)^d} \int \mathrm{d}\boldsymbol{k} \mathrm{e}^{\mathrm{i}\boldsymbol{k}\boldsymbol{y}} f(\boldsymbol{x}, \boldsymbol{k}, t), \tag{5}$$

where $\hbar$ is the reduced Planck constant, m is the mass and $\hat{f}(\boldsymbol{x}, \boldsymbol{y}, t)$ is just $\rho(\boldsymbol{x} + \boldsymbol{y}/2, \boldsymbol{x} - \boldsymbol{y}/2)$. Here, Θ_V is the so-called nonlocal pseudo-differential operator containing all the quantum interference information and has different but equivalent expressions [27].

This paper focuses on the class of $d = 2$, i.e., quantum systems under general 2-D potentials. For a general 2-D smooth potential $V(x_1, x_2)$, we can always have the following decomposition

$$V(x_1, x_2) = \sum_q V_{q,1}(x_1) V_{q,2}(x_2) \tag{6}$$

via the Taylor expansion, which is a linear superposition of a series of products of two 1-D potentials, and each 1-D potential can be further split into a polynomial (pol) one plus a localized (loc) one [27]. That is, each product component $V_1(x_1)V_2(x_2)$ (the subscript q in Eq. (6) is neglected for simplicity) can be expressed as

$$\begin{aligned} V_1(x_1)V_2(x_2) = & V_{1,loc}(x_1)V_{2,loc}(x_2) \\ & + V_{1,loc}(x_1)V_{2,pol}(x_2) + V_{1,pol}(x_1)V_{2,loc}(x_2) \\ & + V_{1,pol}(x_1)V_{2,pol}(x_2), \end{aligned} \tag{7}$$

giving rise to three types of products of 1-D potentials which will be discussed in details below.

- **Type 1:** $V(x_1, x_2) = V_{1,loc}(x_1)V_{2,loc}(x_2)$, $V_{1,loc}(x_1) \in L^1(\mathbb{R})$, $V_{2,loc}(x_2) \in L^1(\mathbb{R})$.
  The pseudo-differential term can be characterized by a convolution form [26]

$$\Theta_V[f](\boldsymbol{x}, \boldsymbol{k}, t) = \int \mathrm{d}\boldsymbol{k}' f(\boldsymbol{x}, \boldsymbol{k}, t) V_w(\boldsymbol{x}, \boldsymbol{k} - \boldsymbol{k}'), \tag{8}$$

$$V_w(\boldsymbol{x},\boldsymbol{k}) = \frac{1}{\mathbb{i}\hbar(2\pi)^2}\int \mathrm{d}\boldsymbol{y}\, \mathbb{e}^{-\mathbb{i}\boldsymbol{k}\boldsymbol{y}}\left[V(\boldsymbol{x}+\frac{\boldsymbol{y}}{2}) - V(\boldsymbol{x}-\frac{\boldsymbol{y}}{2})\right], \tag{9}$$

where $V_w(\boldsymbol{x},\boldsymbol{k})$ is the so-called Wigner potential or Wigner kernel.

- **Type 2:** $V(x_1,x_2) = V_{1,pol}(x_1)V_{2,loc}(x_2)$, $V_{1,pol}(x_1) \in C^{\omega}(\mathbb{R})$, $V_{2,loc}(x_2) \in L^1(\mathbb{R})$.
  Performing the Taylor series for $V_{1,pol}(x_1 \pm y_1/2)$ at x_1 yields

$$V(\boldsymbol{x}+\frac{\boldsymbol{y}}{2}) - V(\boldsymbol{x}-\frac{\boldsymbol{y}}{2}) = \sum_{l=0}^{+\infty}\frac{y_1^l \nabla_{x_1}^l V_{1,pol}(x_1)}{l!2^l}\left[V_{2,loc}(x_2+\frac{y_2}{2}) - (-1)^l V_{2,loc}(x_2-\frac{y_2}{2})\right],$$

  and substituting above expansion into (4) leads to

$$\Theta_V[f](\boldsymbol{x},\boldsymbol{k},t) = \sum_{l=0}^{+\infty}\frac{\mathbb{i}^l\nabla_{x_1}^l V_{1,pol}(x_1)}{2^l l!}\nabla_{k_1}^l\int \mathrm{d}k_2' V_{w,l}^{(2)}(x_2,k_2-k_2')f(x_1,x_2,k_1,k_2',t), \tag{10}$$

  where we have used properties of the Fourier transformation, and

$$V_{w,l}^{(2)}(x_2,k_2) = \frac{1}{2\pi\mathbb{i}\hbar}\int \mathrm{d}y_2 \mathbb{e}^{-\mathbb{i}k_2y_2}\left[V_{2,loc}(x_2+\frac{y_2}{2}) - (-1)^l V_{2,loc}(x_2-\frac{y_2}{2})\right].$$

  Here we adopt the compact notations: $\nabla_{x_1}^l = \partial^l/\partial x_1^l$ and $\nabla_{k_1}^l = \partial^l/\partial k_1^l$ for $l \in \mathbb{N}$.
- **Type 3:** $V(x_1,x_2) = V_{1,pol}(x_1)V_{2,pol}(x_2)$, $V_{1,pol}(x_1) \in C^{\omega}(\mathbb{R})$, $V_{2,pol}(x_2) \in C^{\omega}(\mathbb{R})$.
  Substituting the Taylor series for both $V(x_1+y_1/2, x_2+y_2/2)$ and $V(x_1-y_1/2, x_2-y_2/2)$ at (x_1,x_2) into (4) leads to a Moyal expansion

$$\Theta_V[f](\boldsymbol{x},\boldsymbol{k},t) = \frac{2}{\mathbb{i}\hbar}\sum_{l_1+l_2=\mathrm{odd}}^{+\infty}\frac{\mathbb{i}^{l_1+l_2}}{2^{l_1+l_2}l_1!l_2!}\frac{\partial^{l_1+l_2}}{\partial x_1^{l_1}\partial x_2^{l_2}}V(\boldsymbol{x})\frac{\partial^{l_1+l_2}}{\partial k_1^{l_1}\partial k_2^{l_2}}f(\boldsymbol{x},\boldsymbol{k},t), \tag{11}$$

  which only consists of differential terms.

It can be readily verified that the 2-D double-slit potential in Eq. (1) falls into the second type, and then Eq. (10) becomes

$$\Theta_V[f](\boldsymbol{x},\boldsymbol{k},t) = \sum_{l=0}^{4}\frac{\mathbb{i}^l\nabla_{x_1}^l V_{pol}(x_1)}{2^l l!}\nabla_{k_1}^l\int \mathrm{d}k_2' V_{w,l}^{loc}(x_2,k_2-k_2')f(x_1,x_2,k_1,k_2',t). \tag{12}$$

Obviously, the series now reduces to a finite one which can be readily resolved by standard numerical techniques. Considering the fact that Eq. (12) or Eq. (10) was obtained in the same spirit of the technique used in deriving the Moyal expansion (11), we still call it as the 'Moyal expansion' for simplicity.

A Gaussian barrier

$$V(x_1,x_2) = \mathbb{e}^{-x_2^2/2} \tag{13}$$

belongs to the first type, and a 2-D isotropic harmonic potential

$$V(x_1,x_2) = \frac{1}{2}(x_1^2+x_2^2) \tag{14}$$

the third type. Both of them will be used to benchmark the accuracy of the proposed scheme in Section 5.

The double-slit setup with a central splitter plate in the front, displayed in the right plot of Fig. 1, can be modeled by the general form (6), and its specific form is

$$V(x_1,x_2) = 0.07(x_1^2-5^2)^2\mathbb{e}^{-x_2^2/2} + 10\mathbb{e}^{-4x_1^2}\mathbb{e}^{-(x_2+5)^2/4}. \tag{15}$$

Before we proceed, two remarks on the linearity of the Wigner equations will be highlighted. Such a fundamental property has some direct and useful consequences for our study of the double slit interferences.

(C1) The solution of the Wigner equation with a mixed state $\sum_i p_i f_i(\boldsymbol{x},\boldsymbol{k},0)$ as initial condition has the form $f(\boldsymbol{x},\boldsymbol{k},t) = \sum_i p_i f_i(\boldsymbol{x},\boldsymbol{k},t)$, where $f_i(\boldsymbol{x},\boldsymbol{k},t)$ refers to the solution of the Wigner equation with $f_i(\boldsymbol{x},\boldsymbol{k},0)$ as initial data. This fact implies that if there exists a $f_i(\boldsymbol{x},\boldsymbol{k},0)$ containing the interference, then $f(\boldsymbol{x},\boldsymbol{k},t)$ should carry on such interference, otherwise there should no inference in $f(\boldsymbol{x},\boldsymbol{k},t)$. An example on this point is given in Section 6.5.

(C2) The solution of the Wigner equation with a 2-D potential $V(x_1,x_2) = V_1(x_1) + V_2(x_2)$ has the form $f(\boldsymbol{x},\boldsymbol{k},t) = f_1(x_1,k_1,t)f_2(x_2,k_2,t)$, where $f_i(x_i,k_i,t)$ is nothing but the 2-D Wigner function corresponding to the 1-D potential $V_i(x_i)$ for $i = 1,2$. This fact can be used to construct a reference solution for 4-D Wigner equations (see Section 5.2).

3. Numerical scheme

Considering the decay property of the Wigner function when $|\boldsymbol{k}| \to +\infty$, a simple nullification outside a sufficiently large $\boldsymbol{k}$-domain $\mathcal{K}_1 \times \mathcal{K}_2 = [k_{1,\min}, k_{1,\max}] \times [k_{2,\min}, k_{2,\max}]$ is usually adopted [26,27], thus we are in fact solving a $\boldsymbol{k}$-space truncated 4-D Wigner equation

$$\frac{\partial}{\partial t} f(\boldsymbol{x}, \boldsymbol{k}, t) + \frac{\hbar \boldsymbol{k}}{m} \cdot \nabla_{\boldsymbol{x}} f(\boldsymbol{x}, \boldsymbol{k}, t) = g(\boldsymbol{x}, \boldsymbol{k}, t), \tag{16}$$

$$g(\boldsymbol{x}, \boldsymbol{k}, t) = \sum_{l=0}^{P} \frac{\mathbb{i}^l \nabla_{x_1}^l V_{pol}(x_1)}{2^l l!} \nabla_{k_1}^l \int_{\mathcal{K}_2} \mathrm{d}k_2' \tilde{V}_{w,l}^{loc}(x_2, k_2 - k_2') f(x_1, x_2, k_1, k_2', t), \tag{17}$$

$$\tilde{V}_{w,l}^{loc}(x_2, k_2) = \frac{\Delta y_2}{2\pi \mathbb{i}\hbar} \sum_{\zeta_2 = -\infty}^{+\infty} V_l^{dif}(x_2, y_{\zeta_2}) \circledcirc^{-\mathbb{i} k_2 y_{\zeta_2}}, \tag{18}$$

$$V_l^{dif}(x_2, y_{\zeta_2}) = V_{loc}(x_2 + \frac{y_{\zeta_2}}{2}) - (-1)^l V_{loc}(x_2 - \frac{y_{\zeta_2}}{2}), \tag{19}$$

where $\tilde{V}_w^{loc}(x_2, k_2)$ gives a discretized Wigner kernel for the localized potential $V_{loc}(x_2)$ based on the Poisson summation formula [26], P denotes the order of the polynomial potential, and $y_{\zeta_2} = \zeta_2 \Delta y_2$ with Δy_2 being the spacing.

A necessary and sufficient condition for the truncated Wigner equation (16) to conserve the mass has been given in [26] as

$$L_{k_2} \Delta y_2 = 2\pi, \tag{20}$$

where $L_{k_i} = k_{i,\max} - k_{i,\min}$ represents the length of k_i-domain for $i = 1, 2$. The computational domain in $\boldsymbol{x}$-space is denoted by $\mathcal{X}_1 \times \mathcal{X}_2 = [x_{1,L}, x_{1,R}] \times [x_{2,L}, x_{2,R}]$, and the inflow boundary condition will be adopted hereafter at $\boldsymbol{x}$-boundaries [29].

The spectral methods have been used to resolve the oscillation of the Wigner function and the pseudo-differential term with spectral accuracy [29,26,27]. A straightforward extension of these spectral methods combined with an explicit time marching scheme for simulating the double-slit interference experiment is not feasible mainly due to the limitation of time steps. For example, if we use the explicit Euler scheme combined with a plane wave expansion to simulate the double-well potential $V_{pol}(x) = a(x^2 - b^2)^2$, then the imaginary part of the amplification factor of the resulting scheme turns out to be

$$\lambda^{imag} = \frac{1}{\hbar} \left[\frac{\Delta t}{\Delta k} \pi \nabla_x V_{pol}(x) + \frac{\Delta t}{\Delta k^3} \frac{\pi^3}{24} \nabla_x^3 V_{pol}(x) \right], \tag{21}$$

where Δk is the spacing in k-space. The stability condition requires at least $|\lambda^{imag}| \le 1$ and thus leads to

$$\Delta t \le \frac{\hbar}{a} \min\{ \frac{\Delta k}{\pi \max_{x \in \mathcal{X}} \{4x(x^2 - b^2)\}}, \frac{(\Delta k)^3}{\pi^3 \max_{x \in \mathcal{X}} \{x\}} \}. \tag{22}$$

That is, the time step is limited by both $\nabla_x^l V_{pol}(x)$ and $\nabla_k^l f(x, k, t)$ contained in the Moyal expansion. For example, the time step should be less than 6.7191×10^{-7} when the x-domain is set to be $\mathcal{X} = [-30, 30]$, $\Delta k = 0.05$, $a = 0.2$, $b = 3$, and $\hbar = 1$. Such a small time step is tolerable in 2-D Wigner simulations [29,27], but definitely not for 4-D scenarios [26]. Moreover, the situation becomes worse for the double-slit potential (1) since the fourth derivative shows up (see Remark 1). Namely, substituting the double-slit potential (1) into (17) leads to

$$\begin{aligned} g(\boldsymbol{x}, \boldsymbol{k}, t) =& a(x_1^2 - b^2)^2 G_0(\boldsymbol{x}, \boldsymbol{k}, t) + 2\mathbb{i} a x_1 (x_1^2 - b^2) \nabla_{k_1} G_1(\boldsymbol{x}, \boldsymbol{k}, t) \\ & - \frac{a(3x_1^2 - b^2)}{2} \nabla_{k_1}^2 G_2(\boldsymbol{x}, \boldsymbol{k}, t) - \frac{\mathbb{i} a x_1}{2} \nabla_{k_1}^3 G_3(\boldsymbol{x}, \boldsymbol{k}, t) \\ & + \frac{a}{16} \nabla_{k_1}^4 G_4(\boldsymbol{x}, \boldsymbol{k}, t), \end{aligned} \tag{23}$$

where $G_l(\boldsymbol{x}, \boldsymbol{k}, t)$ is short for $\int_{\mathcal{K}_2} \mathrm{d}k_2' \tilde{V}_{w,l}^{loc}(x_2, k_2 - k_2') f(x_1, x_2, k_1, k_2', t)$. In this work, we will use instead an operator splitting technique and the resulting numerical scheme for the sub-problem containing the Moyal expansion (23) will be shown to be unconditionally stable in the L^2-norm.

3.1. Operator splitting

By defining two operators $\mathcal{A}$ and $\mathcal{B}$ as

$$\begin{aligned} \mathcal{A} f(\boldsymbol{x}, \boldsymbol{k}, t) &:= -\frac{\hbar \boldsymbol{k}}{m} \cdot \nabla_{\boldsymbol{x}} f(\boldsymbol{x}, \boldsymbol{k}, t), \\ \mathcal{B} f(\boldsymbol{x}, \boldsymbol{k}, t) &:= g(\boldsymbol{x}, \boldsymbol{k}, t), \end{aligned} \tag{24}$$

the Wigner equation (16) can be expressed as

$$\frac{\partial}{\partial t} f(\boldsymbol{x}, \boldsymbol{k}, t) = (\mathcal{A} + \mathcal{B}) f(\boldsymbol{x}, \boldsymbol{k}, t), \tag{25}$$

which can be split into the following two sub-equations in an alternating direction manner

$$\begin{cases} \text{(A)} \quad \dfrac{\partial}{\partial t} f(\boldsymbol{x}, \boldsymbol{k}, t) = \mathcal{A} f(\boldsymbol{x}, \boldsymbol{k}, t) = -\dfrac{\hbar \boldsymbol{k}}{m} \cdot \nabla_{\boldsymbol{x}} f(\boldsymbol{x}, \boldsymbol{k}, t), \\ \text{(B)} \quad \dfrac{\partial}{\partial t} f(\boldsymbol{x}, \boldsymbol{k}, t) = \mathcal{B} f(\boldsymbol{x}, \boldsymbol{k}, t) = g(\boldsymbol{x}, \boldsymbol{k}, t), \end{cases} \tag{26}$$

where the sub-equation (A) (resp. sub-equation (B)) only involves an approximation in $\boldsymbol{x}$-direction (resp. $\boldsymbol{k}$-direction).

Specifically, an s-stage exponential operator splitting method for the evolution equation (25) reads

$$f^{n+1}(\boldsymbol{x}, \boldsymbol{k}) = \mathrm{e}^{\Delta t(\mathcal{A}+\mathcal{B})} f^n(\boldsymbol{x}, \boldsymbol{k}) = \prod_{j=1}^{s} \mathrm{e}^{a_j \Delta t \mathcal{A}} \mathrm{e}^{b_j \Delta t \mathcal{B}} f^n(\boldsymbol{x}, \boldsymbol{k}) + \mathcal{O}(\Delta t^{s+1}), \tag{27}$$

where $f^n(\boldsymbol{x}, \boldsymbol{k}) := f(\boldsymbol{x}, \boldsymbol{k}, t^n)$ is the exact solution at time $t^n := n\Delta t$. Setting $s = 2$, $a_1 = a_2 = 1/2$, $b_1 = 1$ and $b_2 = 0$ leads to the well-known second-order Strang method [30]. To match with the spectral accuracy in $(\boldsymbol{x}, \boldsymbol{k})$-space, we adopt here a fourth-order splitting scheme [31] defined by $s = 4$ and

$$a_1 = a_4 = \frac{1}{2\left(2 - \sqrt[3]{2}\right)}, \quad a_2 = a_3 = \frac{1 - \sqrt[3]{2}}{2\left(2 - \sqrt[3]{2}\right)},$$
$$b_1 = b_3 = \frac{1}{2 - \sqrt[3]{2}}, \quad b_2 = -\frac{\sqrt[3]{2}}{2 - \sqrt[3]{2}}, \quad b_4 = 0.$$

The remaining task is to determine the operators $\mathrm{e}^{\Delta t \mathcal{A}}$ and $\mathrm{e}^{\Delta t \mathcal{B}}$, i.e., the solvers for the sub-equations, respectively.

3.2. Fourier spectral collocation method in $\boldsymbol{k}$-space

In view of the nature of Fourier transformation contained in the pseudo-differential term (see Eq. (18)), we use a Fourier spectral method to solve the sub-equation (B) of (26).

Let $k_{i,j_i} = k_{i,\min} + j_i L_{k_i}/N_i$ denote the N_i uniform collocation points in $\mathcal{K}_i$ with $j_i = 0, 1, \ldots, N_i - 1$ for $i = 1, 2$, and

$$S_{\boldsymbol{N}} = \operatorname{span}\{\psi_{\nu_1}(k_1)\psi_{\nu_2}(k_2), \ \ \nu_i = -N_i/2 + 1, \cdots, N_i/2, \ \ i = 1, 2\},$$
$$\psi_{\nu_i}(k) = \mathrm{e}^{2\pi \mathbb{i} \nu_i (k_i - k_{i,\min})/L_{k_i}}, \ \ i = 1, 2.$$

Then, the corresponding interpolation operator $\mathcal{I}_{\boldsymbol{k},\boldsymbol{N}}$ reads

$$\mathcal{I}_{\boldsymbol{k},\boldsymbol{N}} f(\boldsymbol{x}, \boldsymbol{k}, t) = \sum_{\nu_1 = -N_1/2+1}^{N_1/2} \sum_{\nu_2 = -N_2/2+1}^{N_2/2} a_{\nu_1,\nu_2}(\boldsymbol{x}, t) \psi_{\nu_1}(k_1) \psi_{\nu_2}(k_2), \tag{28}$$

$$a_{\nu_1,\nu_2}(\boldsymbol{x}, t) = \frac{1}{N_1 N_2} \sum_{j_1=0}^{N_1-1} \sum_{j_2=0}^{N_2-1} f(\boldsymbol{x}, k_{1,j_1}, k_{2,j_2}, t) \psi_{-\nu_1}(k_{1,j_1}) \psi_{-\nu_2}(k_{2,j_2}). \tag{29}$$

Substituting Eqs. (18), (19) and (28) into the pseudo-differential term (17) yields

$$\begin{aligned} g(\boldsymbol{x}, \boldsymbol{k}, t) \approx & \sum_{l=0}^{P} \frac{\mathbb{i}^l \nabla_{x_1}^l V_{pol}(x_1)}{2^l l! \mathbb{i} \hbar L_{k_2}} \nabla_{k_1}^l \int_{\mathcal{K}_2} \mathrm{d}k_2' \sum_{\zeta_2 = -\infty}^{+\infty} V_l^{dif}(x_2, y_{\zeta_2}) \mathrm{e}^{-\frac{2\pi \mathbb{i} \zeta_2 (k_2 - k_2')}{L_{k_2}}} \\ & \times \sum_{\nu_1 = -N_1/2+1}^{N_1/2} \sum_{\nu_2 = -N_2/2+1}^{N_2/2} a_{\nu_1,\nu_2}(\boldsymbol{x}, t) \psi_{\nu_1}(k_1) \psi_{\nu_2}(k_2') \\ = & \sum_{\nu_1 = -N_1/2+1}^{N_1/2} \sum_{\nu_2 = -N_2/2+1}^{N_2/2} c_{\nu_1,\nu_2}(\boldsymbol{x}) a_{\nu_1,\nu_2}(\boldsymbol{x}, t) \psi_{\nu_1}(k_1) \psi_{\nu_2}(k_2), \end{aligned}$$

$$c_{\nu_1,\nu_2}(\boldsymbol{x}) = -\mathbb{i} \sum_{l=0}^{P} \frac{(-1)^l \nabla_{x_1}^l V_{pol}(x_1)}{l! \hbar} \left(\frac{\pi \nu_1}{L_{k_1}}\right)^l V_l^{dif}(x_2, y_{-\nu_2}),$$

where we have used the relation (20) and the orthogonal relation of the Fourier basis:

$$\int_{\mathcal{K}_2} \mathbb{e}^{2\pi \mathbb{i}(\nu+\zeta)k'/L_k} \mathrm{d}k' = \begin{cases} L_k, & \nu+\zeta=0, \\ 0, & \nu+\zeta\neq 0. \end{cases} \tag{30}$$

Accordingly, the sub-equation (B) in Eq. (26) is approximated by

$$\begin{aligned} &\sum_{\nu_1=-N_1/2+1}^{N_1/2}\sum_{\nu_2=-N_2/2+1}^{N_2/2} \frac{\partial}{\partial t} a_{\nu_1,\nu_2}(\boldsymbol{x},t)\psi_{\nu_1}(k_1)\psi_{\nu_2}(k_2) \\ =&\sum_{\nu_1=-N_1/2+1}^{N_1/2}\sum_{\nu_2=-N_2/2+1}^{N_2/2} c_{\nu_1,\nu_2}(\boldsymbol{x}) a_{\nu_1,\nu_2}(\boldsymbol{x},t)\psi_{\nu_1}(k_1)\psi_{\nu_2}(k_2). \end{aligned}$$

The orthogonal relation (30) further implies

$$\frac{\partial}{\partial t} a_{\nu_1,\nu_2}(\boldsymbol{x},t) = c_{\nu_1,\nu_2}(\boldsymbol{x}) a_{\nu_1,\nu_2}(\boldsymbol{x},t), \quad \nu_i = -\frac{N_i}{2}+1,\ldots,\frac{N_i}{2}, \quad i=1,2, \tag{31}$$

the solution of which has the following explicit form

$$a^{n+1}_{\nu_1,\nu_2}(\boldsymbol{x}) = \mathbb{e}^{c_{\nu_1,\nu_2}(\boldsymbol{x})\Delta t} a^n_{\nu_1,\nu_2}(\boldsymbol{x}). \tag{32}$$

Therefore, staring from the 'initial' data $f^n(\boldsymbol{x},\boldsymbol{k})$ at instant t^n, we are able to obtain the numerical solution of sub-equation (B) in (26) at instant t^{n+1} through first interpolation then evolution:

$$\begin{aligned} F^{n+1}(\boldsymbol{x},\boldsymbol{k}) &= \mathbb{e}^{\Delta t \mathcal{B}} \mathcal{I}_{\boldsymbol{k},\boldsymbol{N}} f^n(\boldsymbol{x},\boldsymbol{k}) \\ &= \sum_{\nu_1=-N_1/2+1}^{N_1/2}\sum_{\nu_2=-N_2/2+1}^{N_2/2} \mathbb{e}^{c_{\nu_1,\nu_2}(\boldsymbol{x})\Delta t} a^n_{\nu_1,\nu_2}(\boldsymbol{x})\psi_{\nu_1}(k_1)\psi_{\nu_2}(k_2), \end{aligned}$$

then that at t^{n+2} and afterwards through only evolution:

$$F^{n+2}(\boldsymbol{x},\boldsymbol{k}) = \mathbb{e}^{\Delta t \mathcal{B}} F^{n+1}(\boldsymbol{x},\boldsymbol{k}). \tag{33}$$

Remark 1. If the explicit Euler time discretization is used to evolve the 4-D Wigner equation (25) with the double-slit potential (1), then the imaginary part of the resulting amplification factor is a diagonal matrix with element being $\lambda^{imag}_{\nu_1,\nu_2} = -\mathbb{i}\Delta t c_{\nu_1,\nu_2}(\boldsymbol{x}_0)$ for a given point $\boldsymbol{x}_0$. Taking a diagonal element with $\nu_1 = N_1/2$, $\nu_2 = N_2/2$ and $\boldsymbol{x}_0 = (x_{1,L}, -N_2\Delta y_2/4)$ as an example, its magnitude reads

$$|\lambda^{imag}_{\frac{N_1}{2},\frac{N_2}{2}}| \approx \frac{a\Delta t}{\hbar}((x^2_{1,L}-b^2)^2 - \frac{2x_{1,L}(x^2_{1,L}-b^2)}{\delta} + \frac{3x^2_{1,L}-b^2}{2\delta^2} - \frac{x_{1,L}}{2\delta^3} + \frac{1}{16\delta^4}), \tag{34}$$

where we have chosen $N_2 = 128$, $\Delta y_2 = 0.5$, $\alpha^2 = 2$, used the approximation $\mathbb{e}^{-(N_2\Delta y_2)^2/(4\alpha^2)} = \mathbb{e}^{-512} \approx 0$, and set $\delta = \Delta k_1/\pi$. The stability condition requires at least $|\lambda^{imag}_{N_1/2,N_2/2}| \le 1$ and thus

$$\Delta t \le \frac{\hbar}{a}\min\{\frac{1}{(x^2_{1,L}-b^2)^2}, \frac{\delta}{-2x_{1,L}(x^2_{1,L}-b^2)}, \frac{2\delta^2}{3x^2_{1,L}-b^2}, \frac{2\delta^3}{-x_{1,L}}, 16\delta^4\}, \tag{35}$$

provided that $x_{1,L} < -|b|$ to guarantee the first four right-hand-side terms of Eq. (34) are all positive. That is, the time step is restricted by both $\nabla^l_{x_1} V_{pol}(x_1)$ and $\nabla^l_{k_1} f(\boldsymbol{x},\boldsymbol{k},t)$ caused by the Moyal expansion, leading to a stricter limitation on the time step which can be unaffordable in actual simulations. For instance, Δt should be less than 4.7065×10^{-7} for $a = 0.2$, $b = 3$, $\hbar = 1$, $x_{1,L} = -30$, and $\Delta k_1 = 0.05$.

Remark 2. It should be pointed out that, the Crank-Nicolson scheme for Eq. (31)

$$a^{n+1}_{\nu_1,\nu_2}(\boldsymbol{x}) = \frac{1+\frac{1}{2}\Delta t c_{\nu_1,\nu_2}(\boldsymbol{x})}{1-\frac{1}{2}\Delta t c_{\nu_1,\nu_2}(\boldsymbol{x})} a^n_{\nu_1,\nu_2}(\boldsymbol{x}) \tag{36}$$

is also unconditionally stable in the L^2-norm, whereas the explicit Euler time discretization is always not.

3.3. Advective method in $(\boldsymbol{x}, t)$-space

We adopt the advective approach [26] to march the sub-equation (A) in Eq. (26) exactly along the characteristic lines as follows

$$f^{n+1}(\boldsymbol{x},\boldsymbol{k}) = \mathbb{e}^{\Delta t\mathcal{A}} f^{n}(\boldsymbol{x},\boldsymbol{k}) = f^{n}(\boldsymbol{x}-\boldsymbol{v}\Delta t,\boldsymbol{k}), \quad \boldsymbol{v} = \frac{\hbar\boldsymbol{k}}{m}. \tag{37}$$

A piecewise cubic spline interpolation with a kind of not-a-knot boundary was used to compute $f^n(\boldsymbol{x}-\boldsymbol{v}\Delta t,\boldsymbol{k},t)$ on the shifted points $(\boldsymbol{x}-\boldsymbol{v}\Delta t,\boldsymbol{k})$ in [26], but failed to handle the inflow boundary condition correctly. To resolve this issue, we turn to a Chebyshev expansion of $f^n(\boldsymbol{x},\boldsymbol{k})$ with respect to $\boldsymbol{x}$, which can handle both the inflow boundary condition and evaluation of function values on the shifted points with higher accuracy [29]. A brief description of the Chebyshev expansion is given below.

The $\boldsymbol{x}$-domain $\mathcal{X}_1\times\mathcal{X}_2$ is divided into $Q_1\times Q_2$ non-overlapping elements as

$$\mathcal{X}_1\times\mathcal{X}_2 = \bigcup_{q_1=1}^{Q_1}\bigcup_{q_2=2}^{Q_2}\mathcal{X}_{1,q_1}\times\mathcal{X}_{2,q_2}, \quad \mathcal{X}_{i,q_i} = [g_{i,q_i-1}, g_{i,q_i}],$$

$$g_{i,0} = x_{i,L}, \quad g_{i,Q_i} = x_{i,R}, \quad g_{i,q_i} = \frac{(x_{i,R}-x_{i,L})}{Q_i}q_i, \quad q_i = 0,1,\ldots,Q_i, \quad i=1,2.$$

The Gauss-Lobatto collocation points are chosen in each $\boldsymbol{x}$-element $\mathcal{X}_{1,q_1}\times\mathcal{X}_{2,q_2}$ $(q_1=1,2,\ldots,Q_1,\ q_2=1,2,\ldots,Q_2)$ as follows

$$x_{q_i,m_i} = g_{i,q_i-1} + \frac{G_{i,q_i}}{2}(1-\cos\frac{m_i\pi}{M_i-1}), \quad m_i = 0,1,\ldots,M_i-1, \tag{38}$$

where $G_{i,q_i} = g_{i,q_i} - g_{i,q_i-1}$ and M_i are the number of collocation points in $\mathcal{X}_{i,q_i}$ for $i=1,2$. Furthermore, for $x_i\in\mathcal{X}_{i,q_i}$, $\eta_i\in[-1,1]$, $\theta_i\in[0,\pi]$, we use the transform

$$x_i = g_{i,q_i-1} + \frac{G_{i,q_i}}{2}(1-\eta_i), \quad \eta_i = \cos(\theta_i)$$

to define

$$\phi_{\mu_i}(x_i) = T_{\mu_i}(\eta_i) = \cos(\mu_i\theta_i), \quad i=1,2.$$

Here, we let

$$S_{\boldsymbol{M}} = \mathrm{span}\{\phi_{\mu_1}(x_1)\phi_{\mu_2}(x_2), \quad \mu_i = 0,1,\cdots,M_i, \quad i=1,2\},$$

and define the interpolation operator

$$\mathcal{I}_{\boldsymbol{x},\boldsymbol{M}} f(\boldsymbol{x},\boldsymbol{k},t) = \sum_{\mu_1=0}^{M_1-1}\sum_{\mu_2=0}^{M_2-1}\beta_{\mu_1,\mu_2}(\boldsymbol{k},t)\phi_{\mu_1}(x_1)\phi_{\mu_2}(x_2). \tag{39}$$

In consequence, staring from the 'initial' data $f^n(\boldsymbol{x},\boldsymbol{k})$ at instant t^n, we are able to obtain the numerical solution of sub-equation (A) in (26) at instant t^{n+1} through first interpolation then evolution:

$$F^{n+1}(\boldsymbol{x},\boldsymbol{k}) = \mathbb{e}^{\Delta t\mathcal{A}}\mathcal{I}_{\boldsymbol{x},\boldsymbol{M}} f^{n}(\boldsymbol{x},\boldsymbol{k}) = I_{\boldsymbol{x},\boldsymbol{M}} f^{n}(\boldsymbol{x}-\boldsymbol{v}\Delta t,\boldsymbol{k}),$$

then that at t^{n+2} and afterwards through only evolution:

$$F^{n+2}(\boldsymbol{x},\boldsymbol{k}) = \mathbb{e}^{\Delta t\mathcal{A}} F^{n+1}(\boldsymbol{x},\boldsymbol{k}) = F^{n+1}(\boldsymbol{x}-\boldsymbol{v}\Delta t,\boldsymbol{k}). \tag{40}$$

Hereafter, we adopt the same mesh in both directions for convenience, say, $N_1 = N_2 := N$ in Eq. (33) and $M_1 = M_2 := M$ in Eq. (39).

4. Numerical analysis

In this section, we would like to study the conservation property, stability, and convergence of the operator splitting method combined the spectral approximation for the 4-D Wigner equation (16), which has been fully described by Eqs. (27), (33) and (40). To this end, it suffices to consider the first order splitting scheme

$$F^{n+1}(\boldsymbol{x},\boldsymbol{k}) = \mathbb{e}^{\Delta t\mathcal{B}}\mathbb{e}^{\Delta t\mathcal{A}} F^{n}(\boldsymbol{x},\boldsymbol{k}), \tag{41}$$

where $F^n(\boldsymbol{x},\boldsymbol{k})\in S_{\boldsymbol{M}}\times S_{\boldsymbol{N}}$ represents the numerical solution of the 4-D Wigner equation (16) at t^n.

Proposition 1. *The operator splitting methods given in (41) conserve the mass, i.e.,*

$$\iint\limits_{\mathcal{X}\times\mathcal{K}} F^{n+1}(\boldsymbol{x},\boldsymbol{k})\mathrm{d}\boldsymbol{x}\mathrm{d}\boldsymbol{k} = \iint\limits_{\mathcal{X}\times\mathcal{K}} F^{n}(\boldsymbol{x},\boldsymbol{k})\mathrm{d}\boldsymbol{x}\mathrm{d}\boldsymbol{k}$$

provided that the total inflow and outflow are in balance. Here $\mathcal{X}=\mathcal{X}_1\times\mathcal{X}_2$ and $\mathcal{K}=\mathcal{K}_1\times\mathcal{K}_2$ denote the computational domains in $\boldsymbol{x}$- and $\boldsymbol{k}$-space, respectively.

Proof. On one hand, according to the same argument used in [26], it can be readily verified that the translation operator $\mathrm{e}^{\Delta t\mathcal{A}}$ defined in Eq. (37) keeps the mass if the total outflow cancels the total inflow. On the other hand, combining the orthogonality of the Fourier basis (see Eq. (30)) and the fact that $c_{0,0}(\boldsymbol{x})\equiv 0$, we can easily obtain that the operator $\mathrm{e}^{\Delta t\mathcal{B}}$ conserves the mass as well. □

Proposition 2. *The spectral scheme (33) for the sub-equation (B) in Eq. (26) is unconditionally stable in the L^2-norm.*

Proof. It can be easily verified that L^2-norm of the amplification factor $\mathrm{e}^{c_{\nu_1,\nu_2}(\boldsymbol{x})\Delta t}$ is always equal to 1 because $c_{\nu_1,\nu_2}(\boldsymbol{x})$ is purely imaginary. That is,

$$||F^{n+1}(\boldsymbol{x},\boldsymbol{k})||_2 = ||\mathrm{e}^{\Delta t\mathcal{B}}F^{n}(\boldsymbol{x},\boldsymbol{k})||_2 = ||F^{n}(\boldsymbol{x},\boldsymbol{k})||_2. \qquad \square \tag{42}$$

Meanwhile, as for the spectral approximation (40) to the sub-equation (B) in Eq. (26), we have $||F^{n+1}(\boldsymbol{x},\boldsymbol{k})||_2 \le ||F^{n}(\boldsymbol{x},\boldsymbol{k})||_2$ as $\mathrm{e}^{\Delta t\mathcal{A}}$ is just a translation operator, if the total inflow is not greater than the total outflow. Combining this fact and Proposition 2 together directly leads to the numerical stability.

Proposition 3. *The operator splitting method (41) is unconditionally stable in the L^2-norm if the total inflow is not greater than the total outflow, namely,*

$$||F^{n+1}(\boldsymbol{x},\boldsymbol{k})||_2 \le ||F^{n}(\boldsymbol{x},\boldsymbol{k})||_2 \tag{43}$$

holds regardless of the mesh size (N, M) and the time step Δt.

Finally, we are able to show the spectral accuracy of the operator splitting scheme (41) with the aid of interpolate estimations [32].

Proposition 4. *Let $f(\boldsymbol{x},\boldsymbol{k},t)$ be the exact solution of Eq. (16), $F^n(\boldsymbol{x},\boldsymbol{k})$ the numerical solution at $t^n=n\Delta t$ obtained by the operator splitting method (41), and $T>0$ a given final time. If $f(\boldsymbol{x},\boldsymbol{k},t)$ is periodic in $\boldsymbol{k}$-space and the total inflow is not greater than the total outflow, we have*

$$||f(\boldsymbol{x},\boldsymbol{k},t^n) - F^n(\boldsymbol{x},\boldsymbol{k})||_2 \le C_t T\Delta t + C_x M^{-m_x} + C_k N^{-m_k}, \quad \forall t^n\in[0,T], \tag{44}$$

where m_x, m_k denote the regularity indexes of the initial data $f(\boldsymbol{x},\boldsymbol{k},t=0)$ in $\boldsymbol{x}$ and $\boldsymbol{k}$, respectively, and C_t, C_x, C_k are some positive constants independent of the mesh size (N, M) and the time step Δt.

Proof. Let $w^{n+1}(\boldsymbol{x},\boldsymbol{k}) = \mathrm{e}^{\Delta t\mathcal{B}}\mathrm{e}^{\Delta t\mathcal{A}}f(\boldsymbol{x},\boldsymbol{k},t^n)$ and $f(\boldsymbol{x},\boldsymbol{k},t^{n+1}) = \mathrm{e}^{\Delta t(\mathcal{B}+\mathcal{A})}f(\boldsymbol{x},\boldsymbol{k},t^n)$. Then it can be easily shown that

$$||f(\boldsymbol{x},\boldsymbol{k},t^{n+1}) - w^{n+1}(\boldsymbol{x},\boldsymbol{k})||_2 \le C_t\Delta t^2,$$

and

$$\begin{aligned}||w^{n+1}(\boldsymbol{x},\boldsymbol{k}) - F^{n+1}(\boldsymbol{x},\boldsymbol{k})||_2 &= ||\mathrm{e}^{\Delta t\mathcal{B}}\mathrm{e}^{\Delta t\mathcal{A}}f(\boldsymbol{x},\boldsymbol{k},t^n) - \mathrm{e}^{\Delta t\mathcal{B}}\mathrm{e}^{\Delta t\mathcal{A}}F^n(\boldsymbol{x},\boldsymbol{k})||_2\\ &\le ||f(\boldsymbol{x},\boldsymbol{k},t^n) - F^n(\boldsymbol{x},\boldsymbol{k})||_2,\end{aligned}$$

where we have applied Eqs. (42) and (43). Thus, using the triangle inequality and by induction, we have

$$\begin{aligned}||f(\boldsymbol{x},\boldsymbol{k},t^n) - F^n(\boldsymbol{x},\boldsymbol{k})||_2 &\le C_t T\Delta t + ||f(\boldsymbol{x},\boldsymbol{k},t^0) - F^0(\boldsymbol{x},\boldsymbol{k})||_2\\ &\le C_t T\Delta t + C_x M^{-m_x} + C_k N^{-m_k},\end{aligned}$$

where $F^0(\boldsymbol{x},\boldsymbol{k}) = \mathcal{I}_{\boldsymbol{x},\boldsymbol{M}}\mathcal{I}_{\boldsymbol{k},\boldsymbol{N}}f(\boldsymbol{x},\boldsymbol{k},t^0)$ and the interpolate estimators for $\mathcal{I}_{\boldsymbol{x},\boldsymbol{M}}, \mathcal{I}_{\boldsymbol{k},\boldsymbol{N}}$ [32] are adopted. □

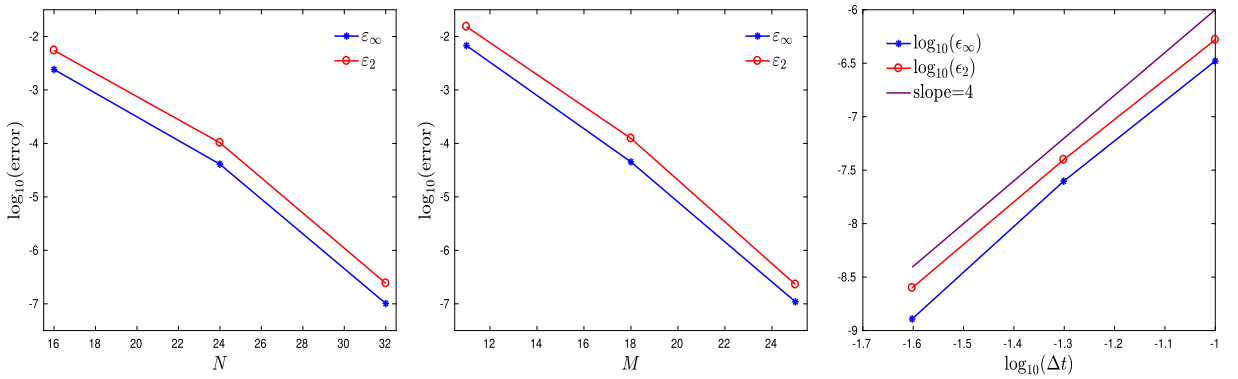

Fig. 2. Harmonic oscillator: The convergence rate with respect to N (left) and M (middle) and the time step Δt (right). The spectral convergence in both $\boldsymbol{k}$-space and $\boldsymbol{x}$-space is evident, and the fourth-order accuracy against the time step is also shown.

5. Accuracy test

In this section, we would like to check the convergence rate of the proposed operator splitting method. A 2-D harmonic oscillator and a Gaussian barrier scattering are used as benchmarks for polynomial potentials and localized potentials, respectively. The L^2-error $\varepsilon_2(t)$ and L^∞-error $\varepsilon_\infty(t)$:

$$\varepsilon_2(t) = \Big(\iint\limits_{\mathcal{X}\times\mathcal{K}} (f^{\text{num}}(\boldsymbol{x},\boldsymbol{k},t) - f^{\text{ref}}(\boldsymbol{x},\boldsymbol{k},t))^2 \mathrm{d}\boldsymbol{x}\mathrm{d}\boldsymbol{k} \Big)^{1/2}, \tag{45}$$

$$\varepsilon_\infty(t) = \max_{(\boldsymbol{x},\boldsymbol{k})\in\mathcal{X}\times\mathcal{K}} \{|f^{\text{num}}(\boldsymbol{x},\boldsymbol{k},t) - f^{\text{ref}}(\boldsymbol{x},\boldsymbol{k},t)|\}, \tag{46}$$

are used to study the convergence rate in terms of the number of collocation points and the time step, and the variation of total mass $\varepsilon_{\text{mass}}(t)$

$$\varepsilon_{\text{mass}}(t) = \iint\limits_{\mathcal{X}\times\mathcal{K}} (f^{\text{num}}(\boldsymbol{x},\boldsymbol{k},t) - f^{\text{num}}(\boldsymbol{x},\boldsymbol{k},0))\mathrm{d}\boldsymbol{x}\mathrm{d}\boldsymbol{k} \tag{47}$$

will monitor the numerical conservation of mass, where f^{num} and f^{ref} denote the numerical solution and reference solution, respectively. The atomic units $\hbar = m = e = 1$ are used if not specified otherwise.

5.1. Harmonic oscillator

The 2-D isotropic harmonic potential (14) is used to benchmark the convergence rate of the proposed method for polynomial potentials because the Wigner function under such a potential has analytical solutions [33,34], which can be used as references to validate numerical results. In fact, the eigenfunctions of the 2-D harmonic oscillator are given by

$$\psi_{n_1,n_2}(x_1,x_2) = \mathrm{e}^{-\frac{1}{2}(x_1^2+x_2^2)} H_{n_1}(x_1) H_{n_2}(x_2), \tag{48}$$

where $H_n(x)$ stands for the Hermite polynomial. We choose the following initial data

$$f_0(\boldsymbol{x},\boldsymbol{k}) = \frac{1}{2\pi^2} \mathrm{e}^{-x_1^2-k_1^2} \mathrm{e}^{-x_2^2-k_2^2} ((1-2x_1^2-2k_1^2)(1-2x_2^2-2k_2^2)+1), \tag{49}$$

which represents a mixed state with a probability of 50% in state $\psi_{00}(x_1,x_2)$ and another 50% in state $\psi_{11}(x_1,x_2)$. Then, we should have a stationary Wigner function, i.e., $f(\boldsymbol{x},\boldsymbol{k},t) \equiv f_0(\boldsymbol{x},\boldsymbol{k})$ at any instant t. Other parameters are chosen as: $-x_{1,L} = x_{1,R} = -x_{2,L} = x_{2,R} = 30$, $-k_{1,\min} = k_{1,\max} = -k_{2,\min} = k_{2,\max} = 2\pi$, and $Q_1 = Q_2 = 10$.

The numerical results are given in Fig. 2, where the left (resp. middle) plot shows clearly the spectral convergence with respect to N (resp. M) while fixing $M = 31$ (resp. $N = 100$) and $\Delta t = 0.02$. Meanwhile, the right plot further displays the fourth-order convergence rate with respect to Δt on a fixed mesh $(N, M) = (64, 31)$. Moreover, the variation of total mass $\varepsilon_{\text{mass}}(\Delta t)$ is 7.8909×10^{-13} even on a rough mesh $(N, M) = (32, 11)$ after one time step. That is, the proposed operator splitting method indeed conserves the mass as predicted by Proposition 1.

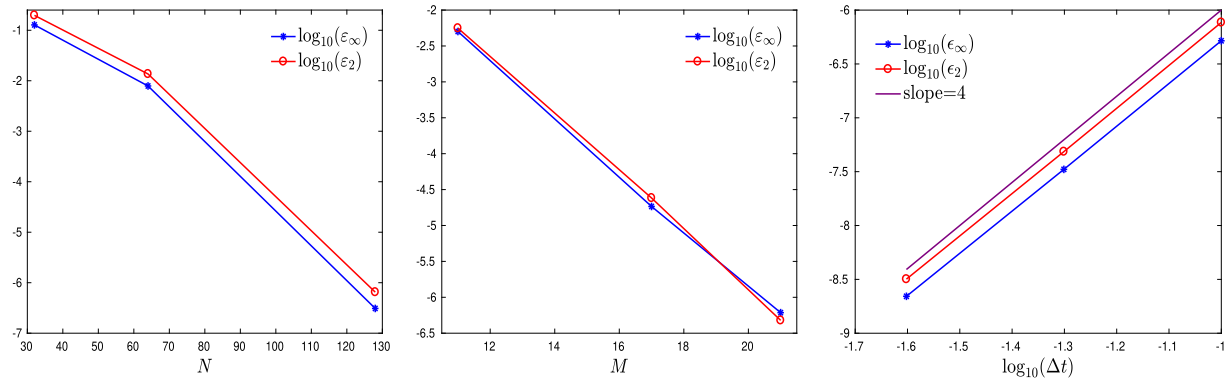

Fig. 3. Gaussian barrier scattering: The convergence rate with respect to N (left) and M (middle) and the time step Δt (right). The spectral convergence in both $\boldsymbol{k}$-space and $\boldsymbol{x}$-space is evident, and the fourth-order accuracy against the time step is also shown.

5.2. Gaussian barrier scattering

We choose the 2-D Gaussian potential (13), which blocks the incident wave only in x_2-space, and a simple product of two Gaussian wave packets [26] to be the initial data:

$$f_0(x_1,x_2,k_1,k_2)=\frac{1}{\pi^2}e^{-\frac{(x_1-x_1^0)^2}{2\sigma_1^2}-2\sigma_1^2(k_1-k_1^0)^2-\frac{(x_2-x_2^0)^2}{2\sigma_2^2}-2\sigma_2^2(k_2-k_2^0)^2}, \tag{50}$$

where x_i^0 is the center of the wave, k_i^0 is the initial wavenumber and σ_i is the minimum position spread for $i=1,2$. Thus, the Gaussian wave packet (13) is a free advection in x_1-space, but will be reflected back in x_2-space. Moreover, according to (C1) in Section 2, the reference 4-D solution for the potential (13) can be constructed from two 2-D Wigner functions, and the latter can be obtained with high accuracy by the spectral element method proposed in [29]. In the numerical simulations, we set the parameters to be $-x_{1,L}=x_{1,R}=-x_{2,L}=x_{2,R}=20$, $-k_{1,\min}=k_{1,\max}=-k_{2,\min}=k_{2,\max}=5\pi/3$, $x_1^0=10$, $x_2^0=-10$, $k_1^0=-1$, $k_2^0=1$, $\sigma_1=\sigma_2=\sqrt{2}$, and $Q_1=Q_2=8$.

To study the convergence rate with respect to N (resp. M), we fix $M=31$ (resp. $N=256$) and $\Delta t=0.01$. The left and middle plots of Fig. 3 also show clearly the spectral convergence with respect to N and M by the proposed method. The right plot of Fig. 3 further displays the fourth-order convergence rate with respect to Δt on a fixed mesh $(N,M)=(160,25)$. The variation of total mass $\varepsilon_{\text{mass}}(\Delta t)$ is 5.5600×10^{-13} on a rough mesh $(N,M)=(32,11)$ after one time step.

6. Double-slit interference experiment

We now turn to the double-slit interference under the 2-D potential (1) in which a and $2b$ determine the width of the two slits and the distance between them, respectively. In optics, the parameters a and b affect the position and intensity of the interference fringe [35]. Four sets of parameters are selected to study the fringe in quantum interference, denoted respectively by

$$\text{(D1)}: a=0.2, b=3; \quad \text{(D2)}: a=0.1, b=4;$$
$$\text{(D3)}: a=0.07, b=5; \quad \text{(D4)}: a=0.05, b=6.$$

The initial Wigner function is still chosen to be the Gaussian wave packet (50) with parameters $k_1^0=0$, $k_2^0=\pi$, $x_1^0=0$, $x_2^0=-10$, $\sigma_1=4$ and $\sigma_2=2$. We further set $\alpha=\sqrt{2}$ in the double-slit potential (1) and $-x_{1,L}=x_{1,R}=-x_{2,L}=x_{2,R}=30$, $-k_{1,\min}=k_{1,\max}=-k_{2,\min}=k_{2,\max}=2\pi$, and $Q=10$.

The spatial marginal distribution

$$F_{sm}(x_1,x_2,t)=\iint\limits_{\mathcal{K}_1\times\mathcal{K}_2} f(x_1,x_2,k_1,k_2,t)\mathrm{d}k_1\mathrm{d}k_2 \tag{51}$$

is used to display the 4-D numerical solutions, and with such spatial marginal distribution, we can calculate the transmission rate $T(t)$ as

$$T(t)=\int\limits_{\mathcal{X}_1}\mathrm{d}x_1\int\limits_0^{x_{2,R}}F_{sm}(x_1,x_2,t)\mathrm{d}x_2, \tag{52}$$

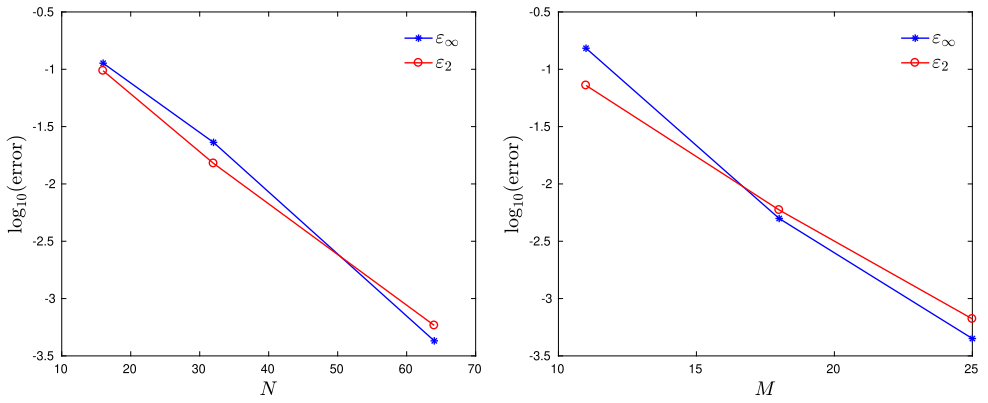

Fig. 4. Double-slit interference: The convergence rate with respect to N (left) and M (right) at the instant $t = 5$. The spectral convergence in both $\boldsymbol{k}$-space and $\boldsymbol{x}$-space is evident.

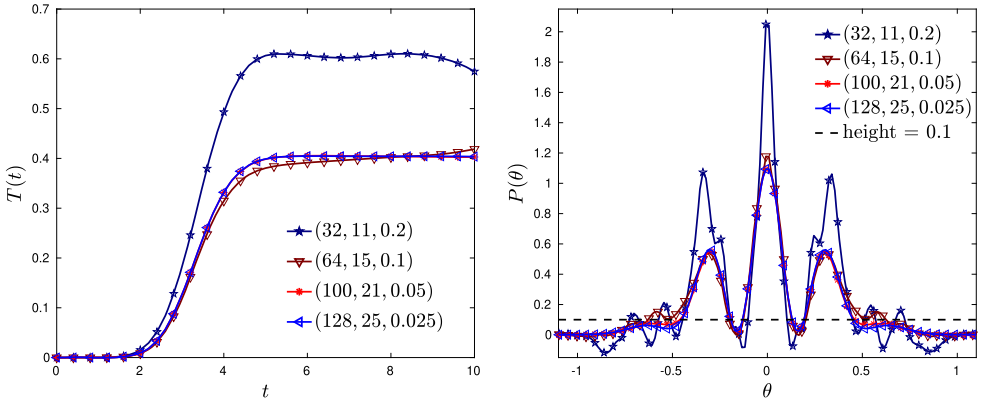

Fig. 5. Double-slit interference: The transmission rate $T(t)$ (left) and the angular distributions $P(\theta)$ (right) at the instant $t = 10$ on four groups of grids: $(N, M, \Delta t) = (100, 11, 0.2)$, $(128, 15, 0.1)$, $(160, 21, 0.05)$ and $(180, 25, 0.025)$.

measuring the probability to find the wave behind the double slits. The quantity also of interest is the angular distribution of the transmitted wave [17],

$$P(\theta, t) = \int_0^{+\infty} F_{sm}(r, \theta, t) r \mathrm{d}r, \tag{53}$$

where $F_{sm}(r, \theta, t)$ gives the spatial marginal distribution (51) under the polar coordinates and $\theta = \arctan(x_1/x_2)$.

6.1. Effect of numerical resolution

In order to test the accuracy of the proposed method for the double-slit potential (1) (i.e., Type 2 in Section 2), a numerical experiment for (D1) is conducted in simulating the double-slit interference for a Gaussian wave packet (50). The numerical solution on the finest mesh $(N, M, \Delta t) = (128, 31, 0.02)$ is chosen to be the reference one and Fig. 4 clearly shows the spectral convergence with respect to N and M.

To show the effect of different numerical resolutions on the interference, we still use (D1) as an example to analyze the numerical results on four different sets of grids: $(N, M, \Delta t) = (32, 11, 0.2)$, $(64, 15, 0.1)$, $(100, 21, 0.05)$ and $(128, 25, 0.025)$. The time taken with 28 CPUs (Intel® Xeon® @ 2.40 GHz) to the instant $t = 10$ on these four sets of grids is about 0.0547 hours, 0.7869 hours, 3.6906 hours and 42.0875 hours, respectively. Fig. 5 depicts the transmission rate $T(t)$ until the instant $t = 10$ and the angular distributions $P(\theta)$ at the final time. It is evident that the numerical result converges as the resolution increases. For example, the relative errors on the value of $T(10)$ are about 42.39%, 3.72% and 0.17% for the first three groups of grids, respectively. More importantly, high resolution plays a key role in capturing both the number and the intensity of the interference fringes. As shown in the right plot of Fig. 5, the number of peaks (each peak corresponds to an interference fringe) with the intensity (height) greater than 0.1 are in order 9, 5, 3, 3 as the grid refines. That is, low resolution computation may produce numerically artificial fringes (which eventually disappears in the converged solution), the positions of which depend on the mesh, for instance, six artificial fringes located at $\theta = \pm 0.7025, \pm 0.5446, \pm 0.2447$ for

the mesh $(32, 11, 0.2)$ and two at $\theta = \pm 0.5762$ for $(64, 15, 0.1)$, whereas the real fringes always stay at the same places regardless of the mesh. However, the intensity of the real fringes may be affected by numerical resolution. Let us take the brightest one (located at $\theta = 0$) as an example. Its intensity is in order 2.0490, 1.1776, 1.0937 and 1.0936 as the resolution increases. In summary, high resolution computation is crucial in accurately capturing correct physical properties of the quantum interference phenomena.

6.2. Effect of double-slit setup

We choose hereafter the mesh to be: $N = 128$, $M = 25$ and $\Delta t = 0.025$. The left plots of Fig. 6 display the curves of transmission rate for the Gaussian wave packet starting from the left and passing through the double-slit potential to the right. These rates at instant $t = 10$ are respectively 0.4036, 0.3303, 0.2491 and 0.1776 for the (D1)-(D4) experiments, and are almost inversely proportional to the distance $2b$ (see the left plot of Fig. 7). In contrast to the exponential decay of the Gaussian wave packet along the x_1-direction, such inverse proportion shows much slower decay and reflects the quantum nature that the interference helps quantum objects travel through the double slits. The middle plots of Fig. 6 show clearly the interference fringes and more details about them can be observed via the angular distributions depicted in the right plots of Fig. 6. It is readily seen there that the number of interference fringes with the intensity greater than 0.1 are 3, 5, 5, 7 for (D1)-(D4), respectively, and the angular distributions of these fringes are all symmetrical with the brightest one located at $\theta = 0$. The intensity (position) of the fringes are: 0.5614 (± 0.3078), 1.0937 (0) for (D1), 0.1767 (± 0.4815), 0.5750 (± 0.2289), 0.8256 (0) for (D2), 0.2306 (± 0.3868), 0.4419 (± 0.1973), 0.5434 (0) for (D3), and 0.1019 (± 0.4973), 0.1973 (± 0.3236), 0.2902 (± 0.1658), 0.3318 (0) for (D4). The right plot of Fig. 7 further presents the curves of position difference between the interference fringes against $1/2b$. We can easily observe there that, the average position difference is approximately proportional to $1/2b$, which is consistent with what happens in classical optics [35], however, both maximum and minimal one show a slight deviation. Moreover, the maximum intensity difference between two adjacent fringes: 0.5523 for (D1), 0.3983 for (D2), 0.2113 for (D3) and 0.0954 for (D4), decreases as the ratio $1/2b$ does.

6.3. Effect of larger mass

This section will study the double-slit interference with larger mass whereas the mass m is 1 in the above experiments. We still use (D1) as an example but the mass is changed to 2 and 5, respectively. The Gaussian wave packet moves more slowly with larger mass, and thus it takes a longer time for it to show the interference. The left plots of Fig. 8 display the transmission rate $T(t)$ until $t = 20$ for $m = 2$ as well as until $t = 50$ for $m = 5$, the middle ones the spatial marginal distribution $F_{sm}(x_1, x_2)$ and the right ones the angular distribution $P(\theta)$ at the final time instant. It can be readily observed there that the interference still happens and there are three fringes in both situations. Their intensity (position) are about 0.5469 (± 0.3078), 0.9456 (0) for $m = 2$, and 0.4488 (± 0.2921), 0.6878 (0) for $m = 5$. In short, the proposed fourth-order 4-D Wigner solver can handle heavier quantum objects as well as longer time quantum dynamics.

6.4. Effect of splitter plate

Recently, a central splitter plate was added in the front of the double-slit and one would ask if the quantum interference is affected by the splitter plate [28]. Within our framework, such double-slit setup with a central splitter plate can be modeled by the general form (6), as shown in Eq. (15), where a splitter plate is added in the front of the double-slit (D3).

To see the effect of the splitter plate, we use the same parameter setup for (D3) above, and the numerical results are displayed in Fig. 9. We can easily observe that the interference still happens in the presence of the splitter plate. Comparing with the results of (D3), the splitter plate strengths the interference by increasing the intensity of the three peaks on the left from 0.2306, 0.4419, 0.5434 to 0.2492, 0.5165, 0.6561, respectively, but without changing their position. This can be readily confirmed in the right plot of Fig. 9 for the angular distribution.

6.5. Comments on the interference of mixed state

Finally, we will apply our numerical methods to simulate the interference of mixed state and as we expected, the quantum interference of mixed state is determined by that of the pure states contained in the mixed state at the initial time. This will demonstrate the superiority of the Wigner formalism, i.e., handling the mixed and pure states on the same footing. To this end, the initial mixed stated we choose is

$$f(\boldsymbol{x}, \boldsymbol{k}) = \frac{1}{2} f_1(\boldsymbol{x}, \boldsymbol{k}) + \frac{1}{2} f_2(\boldsymbol{x}, \boldsymbol{k}), \tag{54}$$

$$f_1(\boldsymbol{x}, \boldsymbol{k}) = \frac{1}{\pi^2} e^{-\frac{(x_1 - x_{11}^0)^2}{2\sigma_1^2} - 2\sigma_1^2 (k_1 - k_{11}^0)^2 - \frac{(x_2 - x_{12}^0)^2}{2\sigma_2^2} - 2\sigma_2^2 (k_2 - k_{12}^0)^2}, \tag{55}$$

$$f_2(\boldsymbol{x}, \boldsymbol{k}) = \frac{1}{\pi^2} e^{-\frac{(x_1 - x_{21}^0)^2}{2\sigma_1^2} - 2\sigma_1^2 (k_1 - k_{21}^0)^2 - \frac{(x_2 - x_{22}^0)^2}{2\sigma_2^2} - 2\sigma_2^2 (k_2 - k_{22}^0)^2}, \tag{56}$$

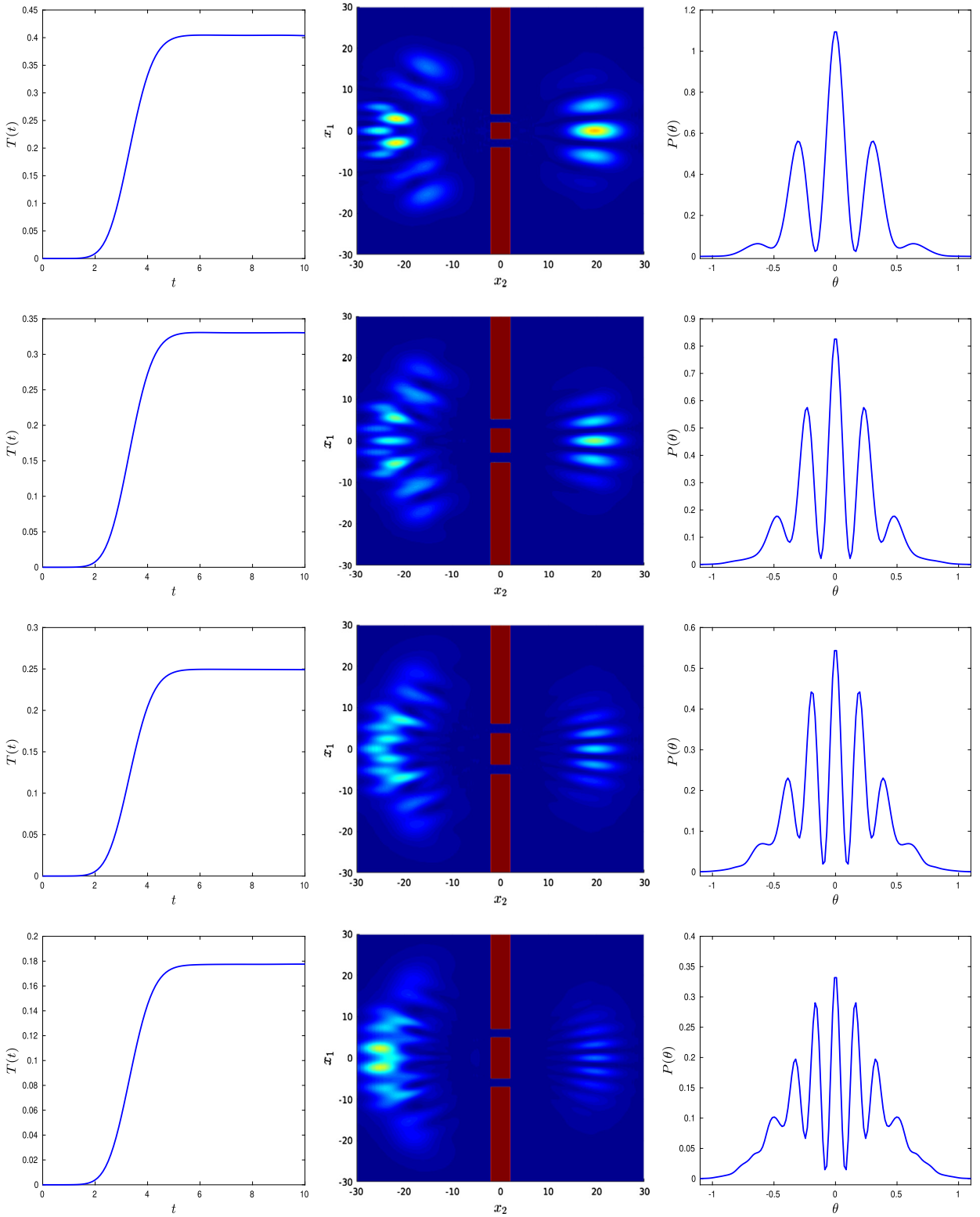

Fig. 6. Double-slit interference: Numerical results for experiments (D1) (first row), (D2) (second row), (D3) (third row) and (D4) (fourth row). The transmission rate $T(t)$ (left) until the instant $t = 10$, the spatial marginal distribution $F_{sm}(x_1, x_2)$ (middle) and the angular distribution $P(\theta)$ (right) at final time $t = 10$ are shown. The red blocks sketch the underlying double-slit potentials by taking into account the position $\pm b$, the width of slits determined by a and b, as well as the width in x_2-direction determined by α (see Eq. (1)). (For interpretation of the colors in the figures, the reader is referred to the web version of this article.)

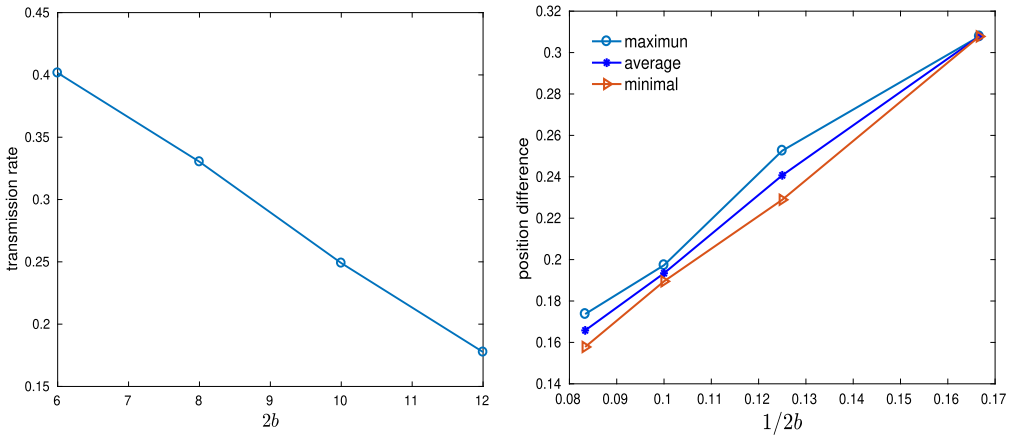

Fig. 7. Double-slit interference: The transmission rate against $2b$ (left) and the position difference between two adjacent fringes against $1/2b$ (right), both of which are measured at $t = 10$. The transmission rate is inversely proportional to the distance $2b$ and the average position difference is shown almost proportional to $1/2b$.

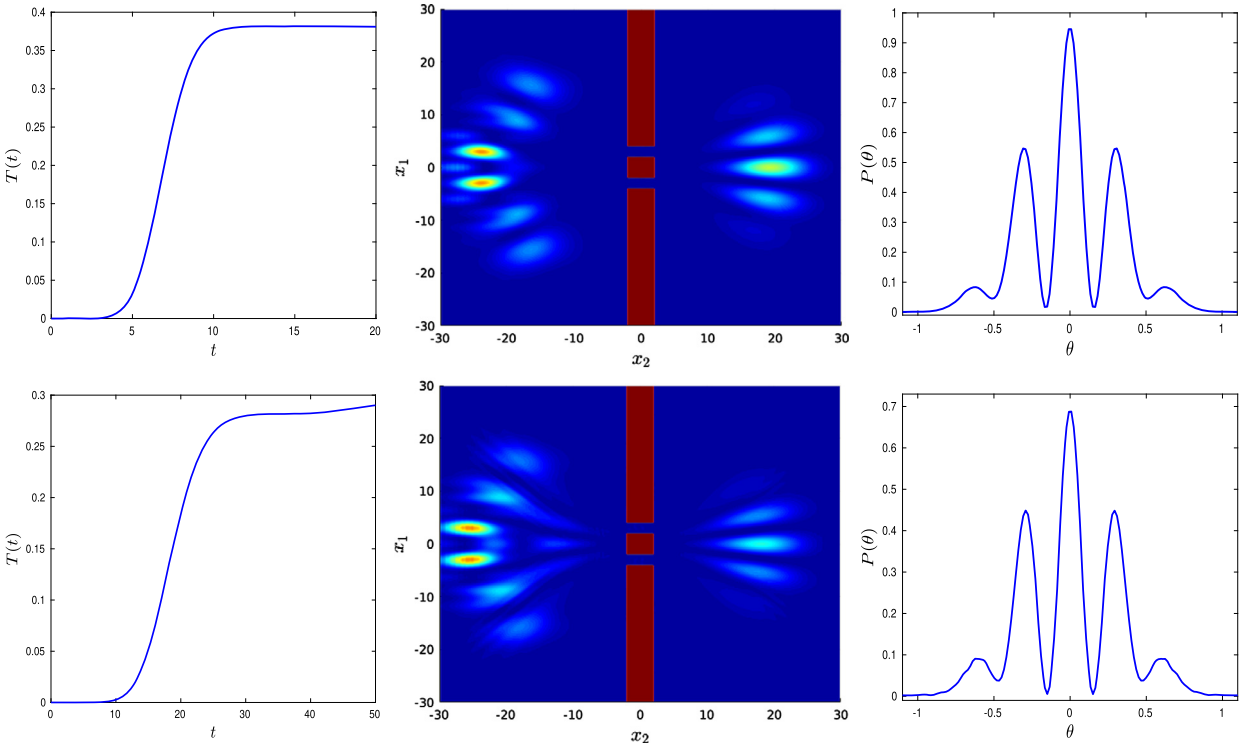

Fig. 8. Double-slit interference: Numerical results of experiment (D1) with $m = 2$ (first row) and $m = 5$ (second row). The transmission rate $T(t)$ (left), the spatial marginal distribution $F_{sm}(x_1, x_2)$ after the collision with the double-slit (middle) and the angular distribution $P(\theta)$ (right) are shown.

and two different parameter setups are:

(P1) $x_{11}^0 = -x_{21}^0 = 3$, $x_{12} = x_{22} = -10$, $k_{11}^0 = k_{21}^0 = 0$, $k_{21} = k_{22} = \pi$, $\sigma_1 = 3$, $\sigma_2 = 3$;
(P2) $x_{11}^0 = -x_{21}^0 = 5$, $x_{12} = x_{22} = -10$, $k_{11}^0 = k_{21}^0 = 0$, $k_{21} = k_{22} = \pi$, $\sigma_1 = 2$, $\sigma_2 = 3$.

The double-slit potential is still set to be (D3). For the parameter setup (P1), the interference for the mixed state appears, and it is expected that the corresponding pure states also have obvious interference fringes after passing through the double-slit, see Fig. 10. However, the interference for a mixed state may not appear and this is exactly what is happening for the parameter setup (P2), see the right plot of Fig. 11. With such parameter setup, the corresponding pure states prefer to travel across the double-slit rather than to show interference, see the left and middle plots of Fig. 11. In fact, as

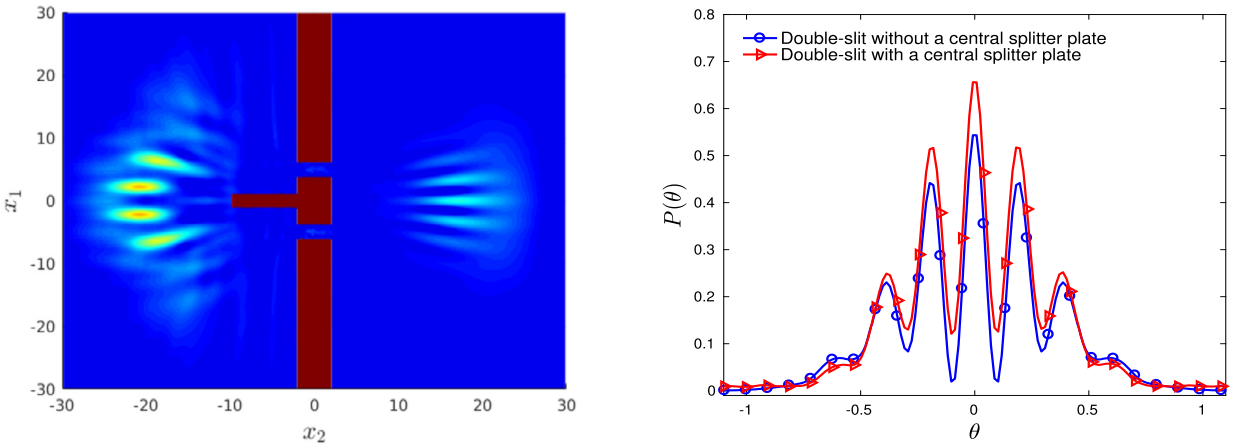

Fig. 9. Double-slit interference with a central splitter plate: The spatial marginal distribution (left) and the angular distribution $P(\theta)$ (right). The results are shown at $t = 10$.

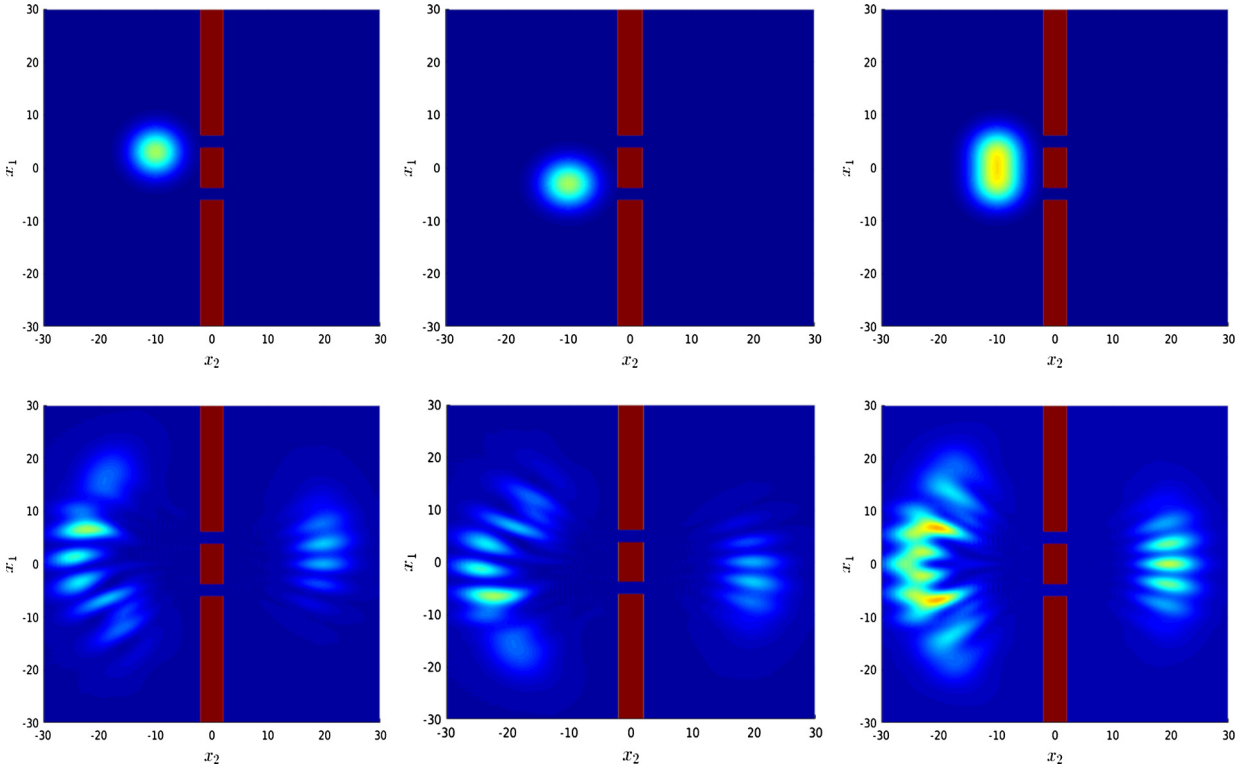

Fig. 10. Simulation of mixed state with parameter setup (P1): The spatial marginal distributions $F_{sm}(x_1, x_2)$ at $t = 0$ (the first row) and $t = 10$ (the second row). The initial data for the left, middle and right plots are given in Eqs. (55), (56) and (54), respectively.

we expected from the statement (C2), the maximum difference: $\max_{\boldsymbol{x}\in\mathcal{X}}\{|F_{sm}^{(mixed)} - (F_{sm}^{(pure1)} + F_{sm}^{(pure2)})/2|\}$, reaches the machine accuracy of 10^{-16} for both parameter sets (P1) and (P2), where the initial data for the spatial marginal distribution $F_{sm}^{(mixed)}$ is given in Eq. (54), while that for $F_{sm}^{(pure1)}$ (resp. $F_{sm}^{(pure2)}$) in Eq. (55) (resp. Eq. (56)).

7. Conclusion

In this paper, we have developed an accurate and efficient numerical method based on an operator splitting for a 4-D Wigner equation and the method is shown to give accurate interference fringes in quantum double-slit experiments. The 4-D Wigner equation was split into two sub-equations which can be handled by a characteristic method for space-time variables and a plane wave method for momentum-time variables. The splitting approach allows us to handle the strict

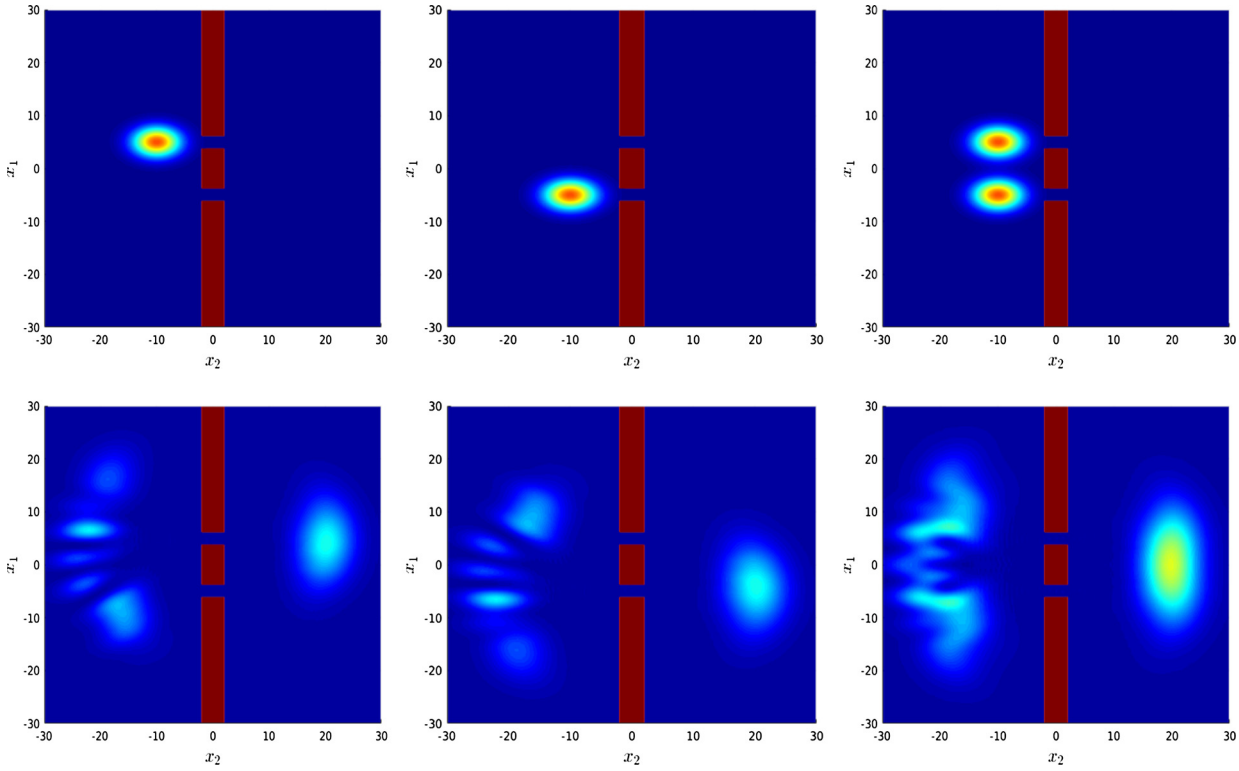

Fig. 11. Simulation of mixed state with parameter setup (P2): The spatial marginal distributions $F_{sm}(x_1, x_2)$ at $t = 0$ (the first row) and $t = 10$ (the second row). The initial data for the left, middle and right plots are given in Eqs. (55), (56) and (54), respectively.

time step restriction from the higher derivatives in the Moyal expansion for the pseudo-differential operator in the Wigner equations. The overall scheme can be accurate to any desired order and conserves mass. Our detailed numerical simulation of the quantum double-slit shows the importance of the proposed high order method in order to produce the correct physical picture of the interference fringes.

Acknowledgements

SS acknowledges the financial support from the National Natural Science Foundation of China (Nos. 11822102, 11421101) and Beijing Academy of Artificial Intelligence (BAAI) as well as the computational resource provided by High-performance Computing Platform of Peking University.

References

[1] R.P. Feynman, R.B. Leighton, M. Sands, The Feynman Lectures on Physics, vol. III: Quantum Mechanics, New Millennium Edition, Basic Books, New York, 2011.
[2] T. Young, II. The Bakerian lecture. On the theory of light and colours, Philos. Trans. R. Soc. Lond. 92 (1802) 12–48.
[3] C. Davisson, L.H. Germer, The scattering of electrons by a single crystal of nickel, Nature 119 (1927) 558–560.
[4] O. Carnal, J. Mlynek, Young's double-slit experiment with atoms: a simple atom interferometer, Phys. Rev. Lett. 66 (1991) 2689.
[5] C. Kurtsiefer, T. Pfau, J. Mlynek, Measurement of the Wigner function of an ensemble of helium atoms, Nature 386 (1997) 150–153.
[6] I. Estermann, O. Stern, Beugung von Molekularstrahlen, Z. Phys. 61 (1930) 95–125.
[7] W. Schöllkopf, J.P. Toennies, Nondestructive mass selection of small van der Waals clusters, Science 266 (1994) 1345–1348.
[8] M. Arndt, O. Nairz, J. Vos-Andreae, C. Keller, G.V.D. Zouw, A. Zeilinger, Wave-particle duality of C_{60}, Nature 401 (1999) 680–682.
[9] O. Nairz, M. Arndt, A. Zeilinger, Quantum interference experiments with large molecules, Am. J. Phys. 71 (2003) 319–325.
[10] B. Thaller, Visual Quantum Mechanics, Springer, New York, 2000.
[11] W.H. Miller, The semiclassical initial value representation: a potentially practical way for adding quantum effects to classical molecular dynamics simulations, J. Phys. Chem. A 105 (2001) 2942–2955.
[12] R. Gelabert, X. Giménez, M. Thoss, H. Wang, W.H. Miller, Semiclassical description of diffraction and its quenching by the forward-backward version of the initial value representation, J. Chem. Phys. 114 (2001) 2572–2579.
[13] M. Gondran, A. Gondran, Numerical simulation of the double slit interference with ultracold atoms, Am. J. Phys. 73 (2005) 507–515.
[14] A.S. Sanz, S. Miret-Artés, A trajectory-based understanding of quantum interference, J. Phys. A, Math. Theor. 41 (2008) 435303.
[15] A.S. Sanz, S. Miret-Artés, A Trajectory Description of Quantum Processes. II. Applications: A Bohmian Perspective, Springer, Heidelberg, 2013.
[16] A. Donoso, C. Martens, Quantum tunneling using entangled classical trajectories, Phys. Rev. Lett. 87 (2001) 223202.
[17] F. Xu, L. Wang, X. Cui, Quantum interference by entangled trajectories, Chin. Phys. Lett. 32 (2015) 080304.
[18] E. Wigner, On the quantum corrections for thermodynamic equilibrium, Phys. Rev. 40 (1932) 749–759.

[19] W.H. Zurek, Sub-Planck structure in phase space and its relevance for quantum decoherence, Nature 412 (2001) 712–717.
[20] D.K. Ferry, M. Nedjakov, The Wigner Function in Science and Technology, IOP Publishing, Bristol, UK, 2018.
[21] W.H. Zurek, Decoherence and the transition from quantum to classical, Phys. Today 44 (1991) 36–44.
[22] C. Zachos, Deformation quantization: quantum mechanics lives and works in phase-space, Int. J. Mod. Phys. A 17 (2002) 297–316.
[23] J.M. Sellier, M. Nedjalkov, I. Dimov, An introduction to applied quantum mechanics in the Wigner Monte Carlo formalism, Phys. Rep. 577 (2015) 1–34.
[24] J. Weinbub, D.K. Ferry, Recent advances in Wigner function approaches, Appl. Phys. Rev. 5 (2018) 041104.
[25] W.B. Case, Wigner functions and Weyl transforms for pedestrians, Am. J. Phys. 76 (2008) 937–946.
[26] Y. Xiong, Z. Chen, S. Shao, An advective-spectral-mixed method for time-dependent many-body Wigner simulations, SIAM J. Sci. Comput. 38 (2016) B491–B520.
[27] Z. Chen, Y. Xiong, S. Shao, Numerical methods for the Wigner equation with unbounded potential, J. Sci. Comput. 79 (2019) 345–368.
[28] A. Andersen, J. Madsen, C. Reichelt, S.R. Ahl, et al., Double-slit experiment with single wave-driven particles and its relation to quantum mechanics, Phys. Rev. E 92 (2015) 013006.
[29] S. Shao, T. Lu, W. Cai, Adaptive conservative cell average spectral element methods for transient Wigner equation in quantum transport, Commun. Comput. Phys. 9 (2011) 711–739.
[30] G. Strang, On the construction and comparison of difference schemes, SIAM J. Numer. Anal. 5 (1968) 506–517.
[31] H. Yoshida, Construction of higher order symplectic integrators, Phys. Lett. A 150 (1990) 262–268.
[32] J. Shen, T. Tang, L. Wang, Spectral Methods: Algorithms, Analysis and Applications, Springer-Verlag, Berlin, 2011.
[33] A.J. Fendrik, M. Bernath, Classical and quantum description of the two-dimensional simple harmonic oscillator in elliptic coordinates, Phys. Rev. A 40 (1989) 4215–4223.
[34] J.P. Dahl, W.P. Schleich, State operator, constants of the motion, and Wigner functions: the two-dimensional isotropic harmonic oscillator, Phys. Rev. A 79 (2009) 024101.
[35] F.A. Jenkins, H.E. White, Fundamentals of Optics, fourth ed., McGraw Hill, New York, 2001.